Seismic Velocities Distribution in a 3D Mantle: Implications for InSight Measurements

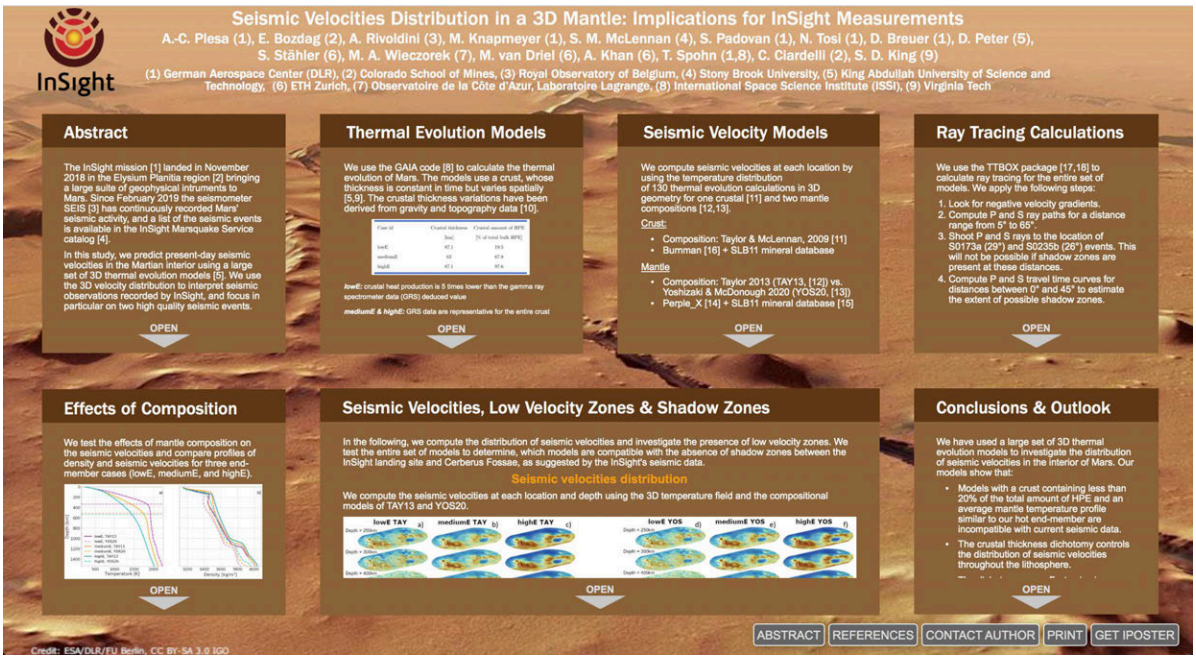

A.-C. Plesa (1), E. Bozdag (2), A. Rivoldini (3), M. Knapmeyer (1),
S. M. McLennan (4), S. Padovan (1), N. Tosi (1), D. Breuer (1), D. Peter (5),
S. Stähler (6), M. A. Wieczorek (7), M. van Driel (6), A. Khan (6),
T. Spohn (1,8), C. Ciardelli (2), S. D. King (9)

(1) German Aerospace Center (DLR), (2) Colorado School of Mines, (3) Royal Observatory of Belgium,
(4) Stony Brook University, (5) King Abdullah University of Science and Technology,
(6) ETH Zurich, (7) Observatoire de la Côte d'Azur, Laboratoire Lagrange,
(8) International Space Science Institute (ISSI), (9) Virginia Tech

PRESENTED AT:

AGU FALL MEETING
Online Everywhere | 1–17 December 2020

ABSTRACT

The InSight mission [1] landed in November 2018 in the Elysium Planitia region [2] bringing a large suite of geophysical intruments to Mars. Since February 2019 the seismometer SEIS [3] has continuously recorded Mars' seismic activity, and a list of the seismic events is available in the InSight Marsquake Service catalog [4].

In this study, we predict present-day seismic velocities in the Martian interior using a large set of 3D thermal evolution models [5]. We use the 3D velocity distribution to interpret seismic observations recorded by InSight, and focus in particular on two high quality seismic events.

The two high quality events S0173a and S0235b have distinguishable P- and S-wave arrivals and are thought to originate in Cerberus Fossae [6], a potentially active fault system [7].

Our results show that these events can be used to place constraints on the thermal state of the lithosphere and on the distribution of heat producing elements (HPE) between the mantle and crust. We expect that future high-quality seismic events have the potential to further constrain the amount of HPE in the Martian crust.

THERMAL EVOLUTION MODELS

We use the GAIA code [8] to calculate the thermal evolution of Mars. The models use a crust, whose thickness is constant in time but varies spatially [5,9]. The crustal thickness variations have been derived from gravity and topography data [10].

Case id	Crustal thickness [km]	Crustal amount of HPE [% of total bulk HPE]
lowE	87.1	19.5
mediumE	62	67.8
highE	87.1	97.6

lowE: crustal heat production is 5 times lower than the gamma ray spectrometer data (GRS) deduced value

mediumE & highE: GRS data are representative for the entire crust

In the lowE model, the crust contains only 19.5% of total amount of heat producing elements (HPE), which leads to a hot end-member mantle temperature.

The crust in the highE model contains 97.6% of the total bulk HPE, leading to cold end-member scenario. The mediumE model is an intermediate case, in which the crust contains 67.8% of the total bulk HPE content. In this case, the mantle temperature lies between that of the cold and hot end-member models.

SEISMIC VELOCITY MODELS

We compute seismic velocities at each location by using the temperature distribution
of 130 thermal evolution calculations in 3D geometry for one crustal [11] and two mantle compositions [12,13].

Crust:

- Composition: Taylor & McLennan, 2009 [11]
- Burnman [14] + SLB11 mineral database [15]

Mantle

- Composition: Taylor 2013 (TAY13, [12]) vs. Yoshizaki & McDonough 2020 (YOS20, [13])
- Perple_X [16] + SLB11 mineral database

The seismic velocities are computed at each location by using the temperature distribution of the 3D models and pre-computed Perple_X tables.

RAY TRACING CALCULATIONS

We use the TTBOX package [17,18] to calculate ray tracing for the entire set of models. We apply the following steps:

1. Look for negative velocity gradients.
2. Compute P and S ray paths for a distance range from 5° to 65°.
3. Shoot P and S rays to the location of S0173a (29°) and S0235b (26°) events. This will not be possible if shadow zones are present at these distances.
4. Compute P and S travel time curves for distances between 0° and 45° to estimate the extent of possible shadow zones.

We compute ray tracing for the entire set of 260 models (130 thermal mocles and 2 mantle compositions). We calculate 1D seismic velocity profiles by averaging our data along a great circle segment between InSight landing site and Cerberus Fossae. The source depths chosen for our analysis are 50, 100, and 150 km, since neither of the events shows a discernible surface wave train.

EFFECTS OF COMPOSITION

We test the effects of mantle composition on the seismic velocities and compare profiles of density and seismic velocities for three end-member cases (lowE, mediumE, and highE).

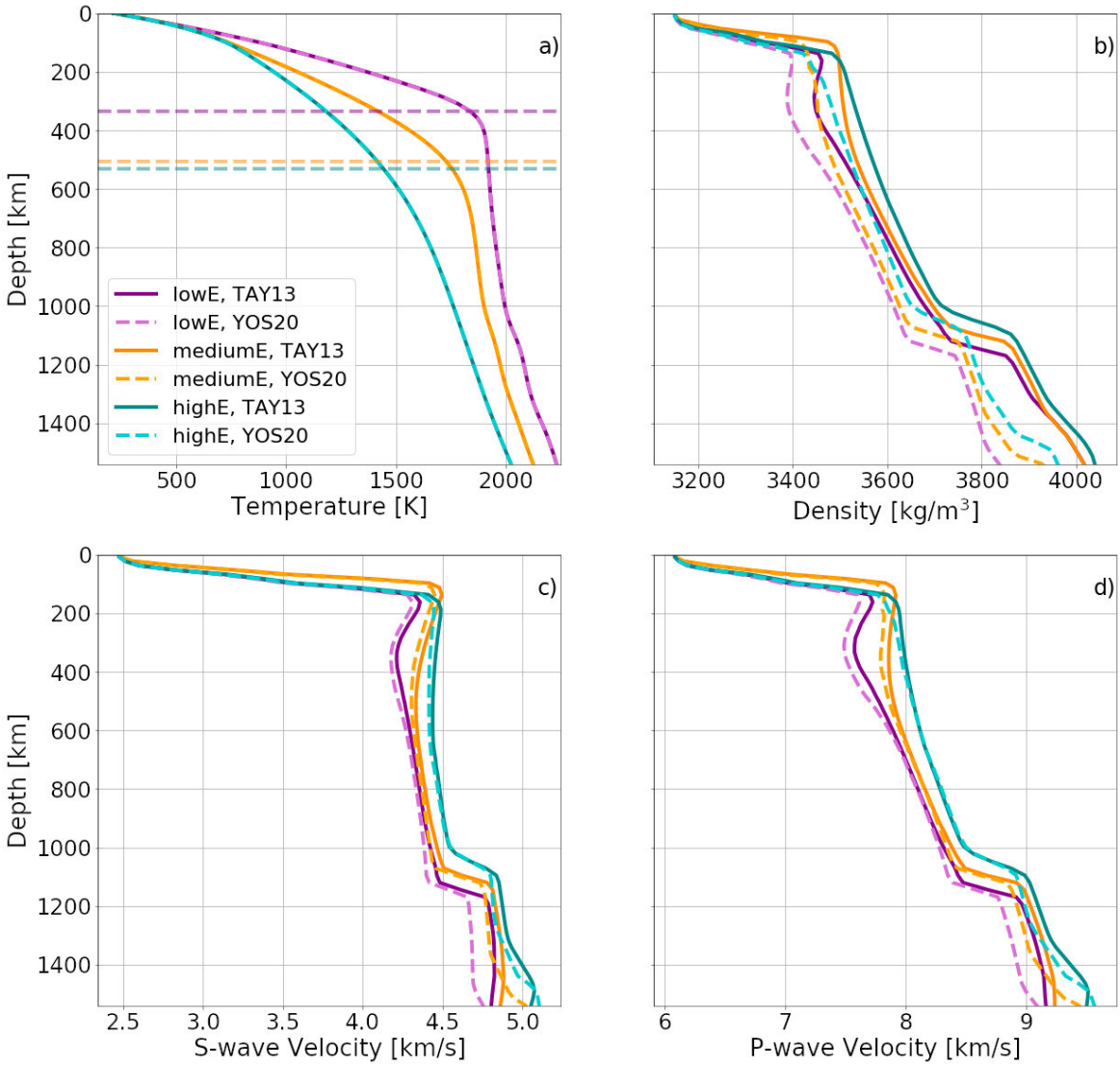

Fig. 1: Results of models comparing the mantle composition of TAY13 and YOS20 for cases lowE, mediumE, and highE: a) the average temperature profiles used as input for the two mantle compositions; b) average density profiles; c) average S-wave velocity and d) average P-wave velocity profiles. The horizontal dashed lines in Panel a) show the average lithosphere thickness of each model. For the crust we used a composition similar to [13].

In the YOS20 compositional model, the lower FeO content (14.7+/-1.0wt%) compared to the value of the TAY13 model (18.1+/-2.2 wt%) leads in lower densities and slightly lower seismic velocities in the Martian mantle. The horizontal dashed lines on Fig1a) indicate the average lithosphere thickness that was computed using the depth at which the temperature gradient drops below 1 K/km.

The phase diagrams computed below the crust for the TAY13 and YOS20 compositions show the depth and the proportion of stable mineral phases that were obtained when using a hot (lowE), intermediate (mediumE), and cold (highE) average temperature profiles.

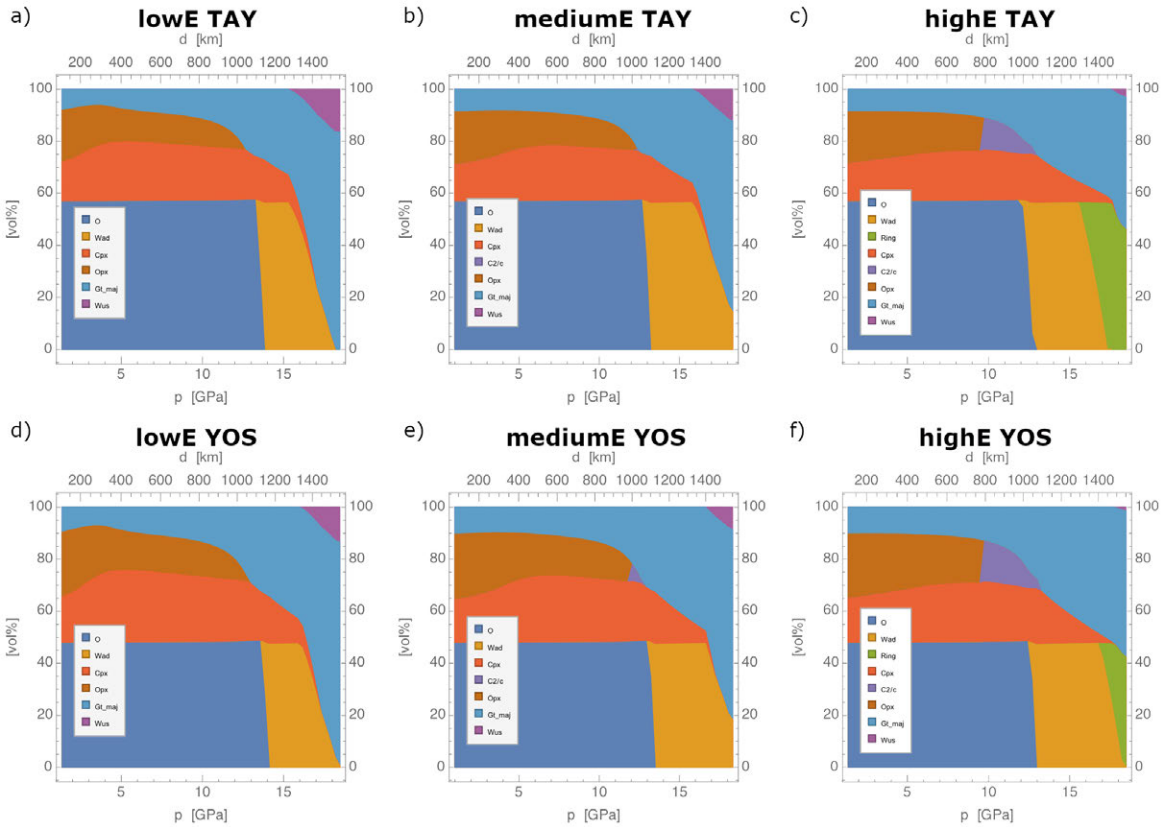

Fig. 2: Phase diagrams computed below the crust for the mantle composition of TAY13 (top row) and YOS20 (bottom row). Panels a) and d) show the phase diagrams for TAY13 and YOS20, respectively for the hot end-member, low amount of crustal HPE case (lowE). Panels b) and e) show the phase diagrams for the intermediate thermal profile (mediumE), while panels c) and f) show the stable mineral phases obtained for the cold end-member, high amount of crustal HPE case (highE).

For both TAY13 and YOS20 compositional models, the pressure, at which the olivine to wadsleite phase transition takes place, is around 13 GPa (about 1000 km depth) in the cold temperature case (highE). The depth of this phase transition increases with increasing temperature, and lies at about 1070 km depth for mediumE and 1120 km depth for lowE, respectively. This phase transition is the most prominent one and is observed both in density and seismic velocities.

SEISMIC VELOCITIES, LOW VELOCITY ZONES & SHADOW ZONES

In the following, we compute the distribution of seismic velocities and investigate the presence of low velocity zones. We test the entire set of models to determine, which models are compatible with the absence of shadow zones between the InSight landing site and Cerberus Fossae, as suggested by the InSight's seismic data.

Seismic velocities distribution

We compute the seismic velocities at each location and depth using the 3D temperature field and the compositional models of TAY13 and YOS20.

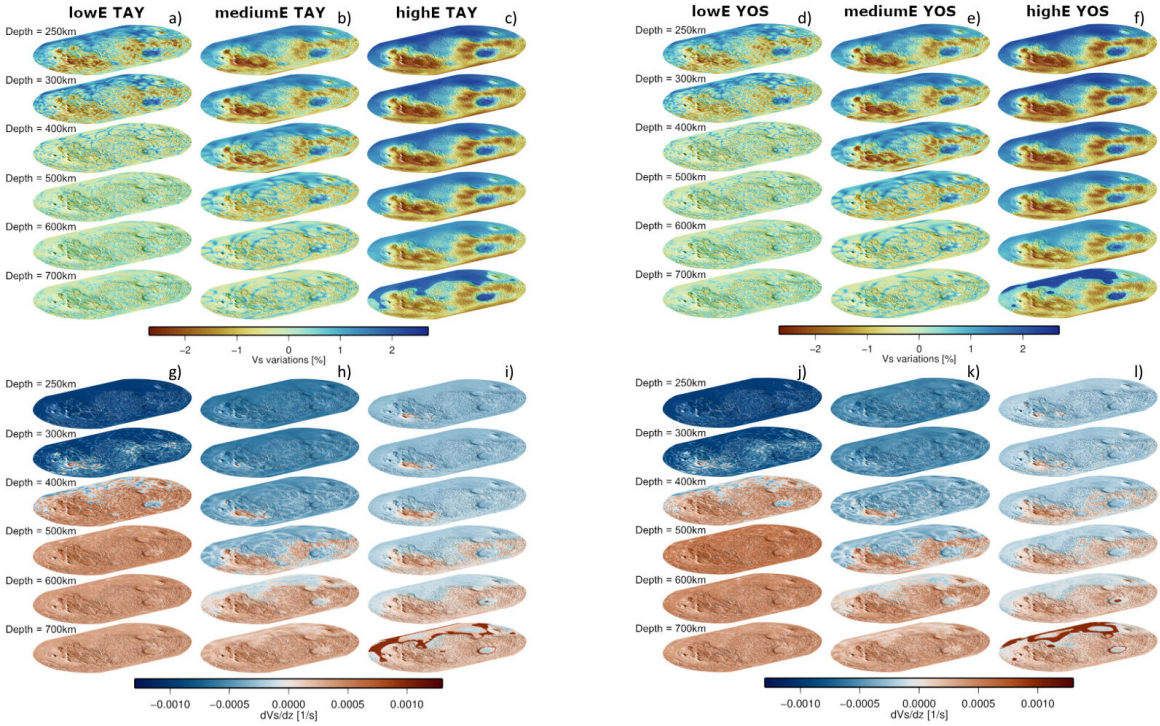

Fig. 3: Top panels show the shear wave velocity distribution at various depths in the Martian mantle for the lowE, mediumE, and highE models and for TAY13 (a,b,c) and YOS20 (d,e,f) compositions. The lower panels show the shear wave velocity gradient. Negative values of the S-wave velocity gradient show the location of low velocity zones. We note, however, that a negative gradient does not necessarily indicate a shadow zone. For both TAY13 and YOS20 compositions, a phase transition in the pyroxene system (orthopyroxene to C2/c clinopyroxene) takes place in the highE model (cold end-member) around 600 - 700 km depth. This is indicated by high S-wave velocity gradients, as the S-wave velocity changes significantly over a small depth interval.

Low velocity zones distribution

We analyze the presence of low velocity zones for all thermal evolution models using TAY13 and YOS20 mantle compositions:

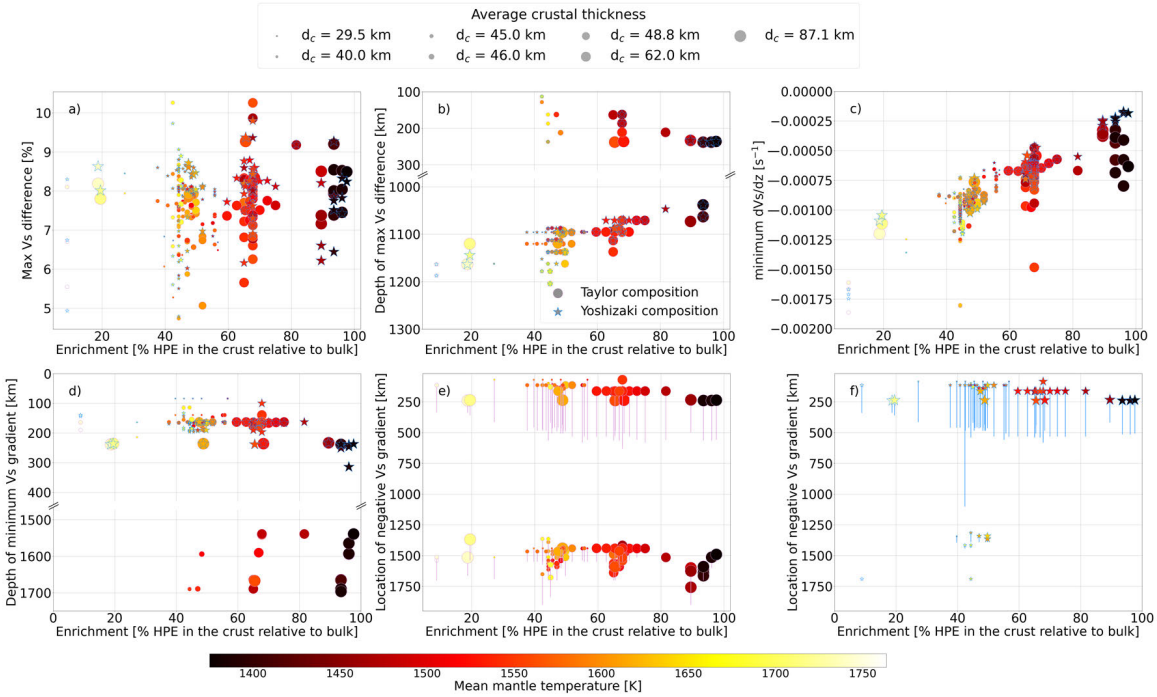

Fig. 4: In panel a) we show the maximum difference between minimum and maximum shear velocity at each depth for TAY13 (circles) and YOS20 (stars) compositions. Panel b) shows the depth at which the maximum difference shown in panel a) was attained. The minimum shear wave velocity gradient computed using the average profile is shown in panel c). In panel d) we calculated the depth at which the minimum shear wave velocity gradient shown in panel c) was attained. The segments in panel e) and f) show the extent of negative shear wave velocity gradient regions, which have been calculated based on the average velocity profile for both TAY13 and YOS20 mantle compositions. Note the broken y-Axis in panels b) and d) that shows the relevant depths.

S-wave shadow zones

We perform ray tracing calculations to determine, which models present shadow zones between the InSight landing site and Cerberus Fossae.

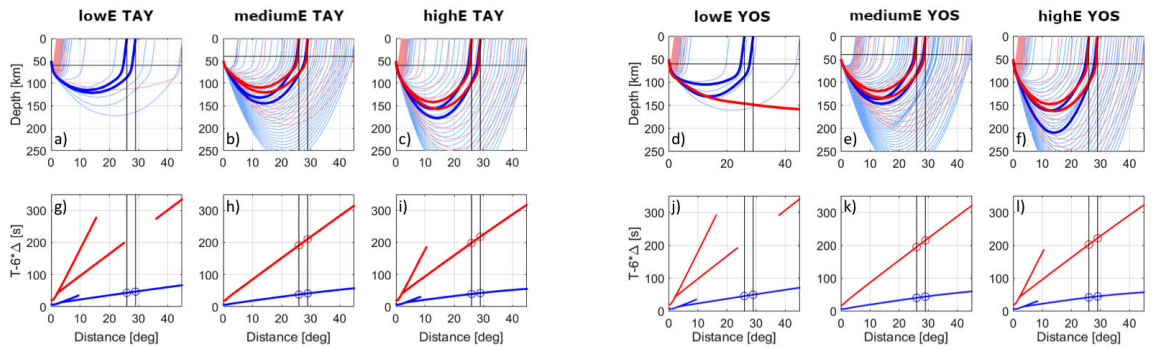

Fig. 5: We use ray tracing calculations to determine if shadow zones are present between InSight location and two high quality events (S0173a and S0235b), for which the source is suggested to lie in Cerberus Fossae. We show a detailed analysis of the lowE, mediumE, and highE models for the TAY13 (left) and YOS20 (right) mantle compositions. The thick blue and red lines in the top panels (a-f) show rays that reach the epicentral distances relevant for the S0173a and S0235b events (i.e., 29° and 26°, respectively). The gap in the lines for the lowE models in the lower panels (g-l) indicate the presence of a shadow zone. The model that employs only a limited amount of HPE in the crust (lowE) is therefore not compatible with InSight observations that show clear S-wave arrivals for S0173a and S0235b.

S-wave shadow zone constraints for thermal evolution models

We use the absence of an S-wave shadow zone between InSight and Cerberus Fossae to reject models that are incompatible with seismic observations.

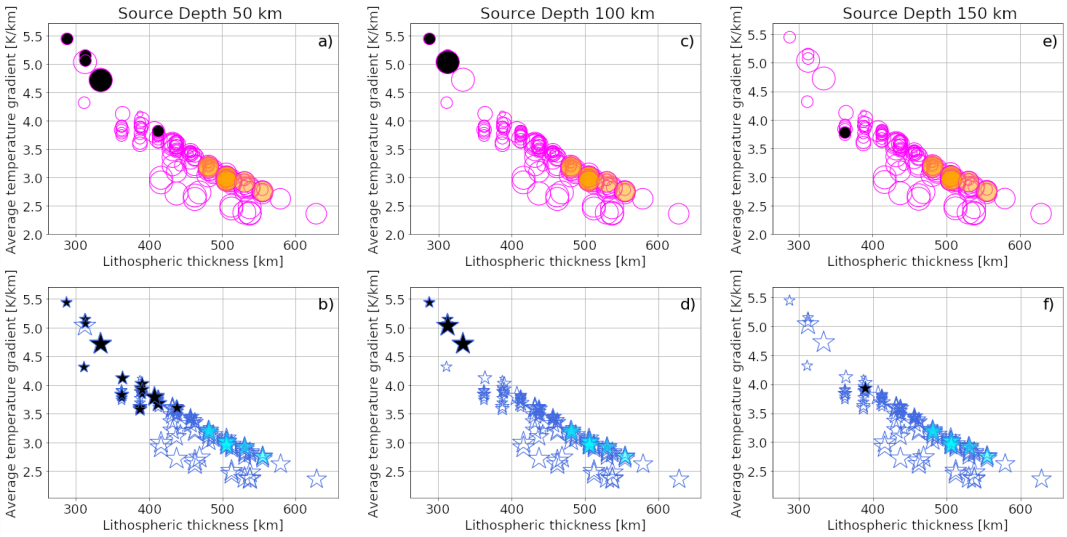

Fig. 6: Models that present shadow zones and, hence, are incompatible with InSight observations are shown by filled black symbols. For comparison, previous best-fit models that match geophysical, geological and petrological constraints [5] are shown by filled colored symbols. The models, which are incompatible with InSight data, have a lithosphere thinner than 450 km on average and a large lithospheric thermal gradient (larger than 3.5 K/km).

CONCLUSIONS & OUTLOOK

We have used a large set of 3D thermal evolution models to investigate the distribution of seismic velocities in the interior of Mars. Our models show that:

- Models with a crust containing less than 20% of the total amount of HPE and an average mantle temperature profile similar to our hot end-member are incompatible with current seismic data.
- The crustal thickness dichotomy controls the distribution of seismic velocities throughout the lithosphere.
- The dichotomy may affect seismic velocities at depths larger than 400 km for models with cold and thick lithospheres.
- Models show large variations of S-wave velocity either below the Moho or at the depth of olivine to wadsleite phase transition.
- Prior knowledge about velocity variations resulting from the olivine to wadsleite phase transition can be used to locate the depth of the transition from seismic data (Huang et al., this meeting) (https://agu.confex.com/agu/fm20/meetingapp.cgi/Paper/680965).

Future work will combine the seismic velocities distribution calculated in this study with modeling of seismic wave propagation [19,20].

ABSTRACT

The InSight mission [1] landed in November 2018 in the Elysium Planitia region [2] bringing the first geophysical observatory to Mars. Since February 2019 the seismometer SEIS [3] has continuously recorded Mars' seismic activity, and a list of the seismic events is available in the InSight Marsquake Service catalog [4].

In this study, we predict present-day seismic velocities in the Martian interior using the 3D thermal evolution models of [5] (Fig. 1a, b). We then use the 3D velocity distributions to interpret seismic observations recorded by InSight. Our analysis is focused on the two high quality events S0173a and S0235b. Both have distinguishable P- and S-wave arrivals and are thought to originate in Cerberus Fossae [6], a potentially active fault system [7].

Our results show that models with a crust containing more than half of the total amount of heat producing elements (HPE) of the bulk of Mars lead to large variations of the seismic velocities in the lithosphere. A seismic velocity pattern similar to the crustal thickness structure is observed at depths larger than 400 km for cases with cold and thick lithospheres. Models, with less than 20% of the total HPE in the crust have thinner lithospheres with shallower but more prominent low velocity zones. The latter, lead to shadow zones that are incompatible with the observed P- and S-wave arrivals of seismic events occurring in Cerberus Fossae, in 20° - 40° epicentral distance (Fig. 1c). We therefore expect that future high-quality seismic events have the potential to further constrain the amount of HPE in the Martian crust.

Future work will combine the seismic velocities distribution calculated in this study with modeling of seismic wave propagation [8, 9] (Fig. 1d). This will help to assess the effects of a 3D thermal structure on the waveforms and provide a powerful framework for the interpretation of InSight’s seismic data.

[1] Banerdt et al., Nat. Geo. 2020; [2] Golombek et al., Nat. Comm. 2020, [3] Lognnoné et al., Nat. Geo. 2020, [4] InSight MQS, Mars Seismic Catalogue, InSight Mission V3, 2020, https://doi.org/10.12686/A8, [5] Plesa et al., GRL 2018, [6] Giardini et al., Nat. Geo. 2020, [7] Taylor et al., JGR 2013, [8] Bozdag et al., SSR 2017, [9] Komatitsch & Tromp, GJI 2002.

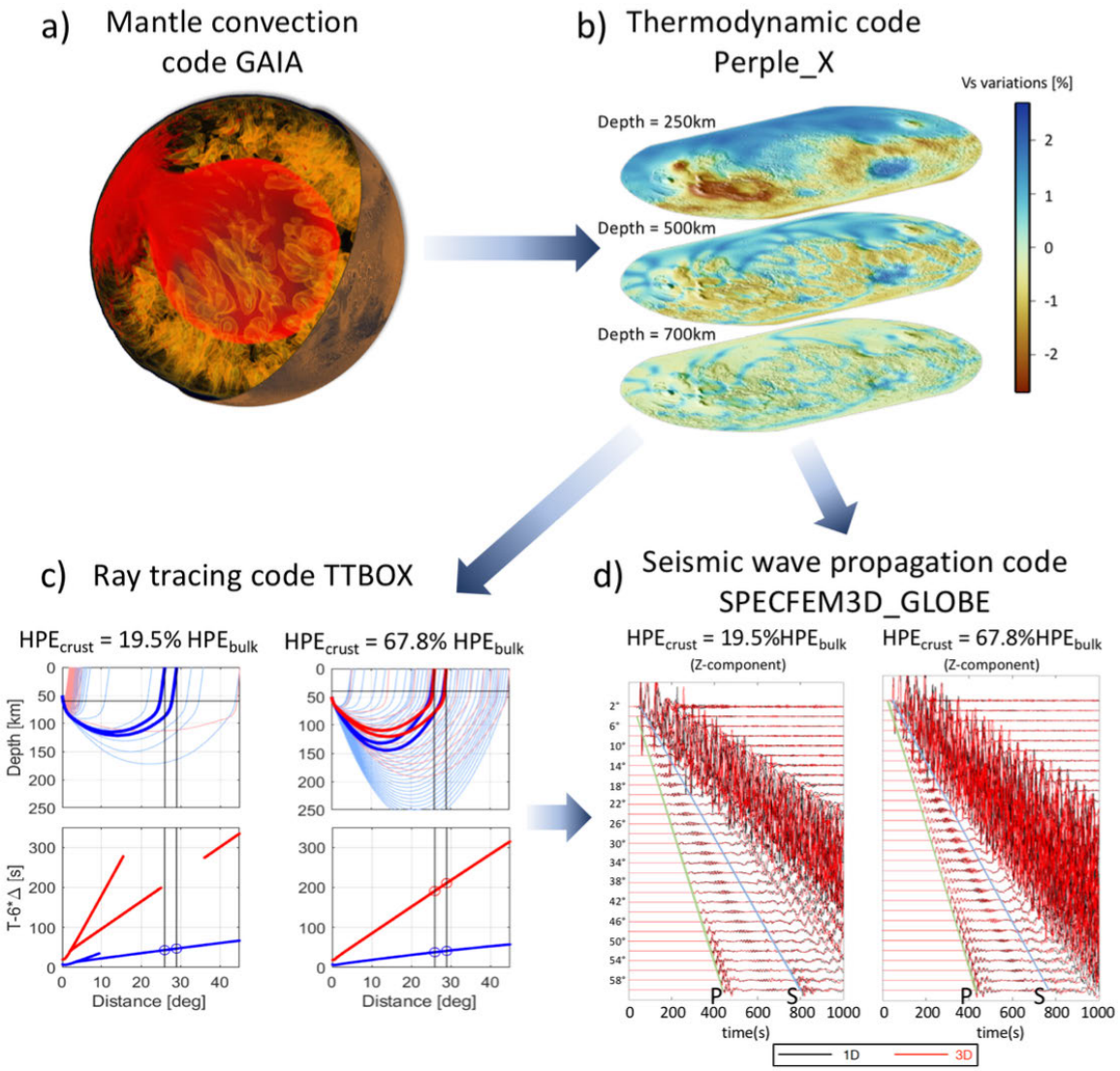

Fig.1: a) Snapshot of the temperature distribution, as obtained from 3D thermal evolution models of the interior of Mars; b) Distribution of present-day seismic velocities calculated based on the temperature distribution from 3D thermal evolution models (Panel a) and using the mineralogical model of (Taylor, Geochem., 2013); c) Ray tracing calculations using averaged seismic velocities between InSight location and Cerberus Fossae that have been calculated from distributions similar to the one shown in Panel b); d) Preliminary waveform calculations using 3D seismic velocity structures similar to the one shown in Panel b) and travel times estimates for P- and S-phase identification from TTBOX (Panel c).
(https://agu.confex.com/data/abstract/agu/fm20/9/0/Paper_726609_abstract_692710_0.png)

REFERENCES

[1] Banerdt, W. B., Smrekar, S. E., Baneld, D., Giardini, D., Golombek, M., Johnson, C. L., . . . others (2020). Initial results from the InSight mission on Mars. Nature Geoscience, 1-7.

[2] Golombek, M., Warner, N., Grant, J., Hauber, E., Ansan, V., Weitz, C., . . . others (2020). Geology of the InSight landing site on Mars. Nature communications, 11(1), 1-11.

[3] Lognonne, P., Banerdt, W., Pike, W., Giardini, D., Christensen, U., Garcia, R., . . . others (2020). Constraints on the shallow elastic and anelastic structure of Mars from InSight seismic data. Nature Geoscience, 13(3), 213-220.

[4] InSight Marsquake Service. (2020). Mars Seismic Catalogue, InSight Mission; V3 2020-07-01. ETHZ, IPGP, JPL, ICL, ISAE-Supaero, MPS, Univ. Bristol. doi: https://doi.org/10.12686/a8

[5] Plesa, A.-C., Padovan, S., Tosi, N., Breuer, D., Grott, M., Wieczorek, M. A., Smrekar, S. E., Banerdt, W. B. (2018). The thermal state and interior structure of Mars. Geophysical Research Letters, 45(22), 12-198.

[6] Giardini, D., Lognonne, P., Banerdt, W. B., Pike, W. T., Christensen, U., Ceylan, S., . . . others (2020). The seismicity of Mars. Nature Geoscience, 13(3), 205-212.

[7] Taylor, J., Teanby, N. A., & Wookey, J.(2013). Estimates of seismic activity in the Cerberus Fossae region of Mars. Journal of Geophysical Research: Planets, 118(12), 2570–2581.

[8] Hüttig, C., Tosi, N., & Moore, W. B. (2013). An improved formulation of the incompressible Navier-Stokes equations with variable viscosity. Physics of the Earth and Planetary Interios, 40, 113–129.

[9] Plesa, A.-C., Grott, M., Tosi, N., Breuer, D., Spohn, T., & Wieczorek, M. A. (2016). How large are present-day heat flux variations across the surface of Mars? Journal of Geophysical Research: Planets, 121(12), 2386-2403.

[10] Wieczorek, M. A., Beuthe, M., Rivoldini, A., & Van Hoolst, T. (2019). Hydrostatic interfaces in bodies with nonhydrostatic lithospheres. Journal of Geophysical Research: Planets, 124(5), 1410-1432.

[11] Taylor, S. R., & McLennan, S. (2009). Planetary crusts: their composition, origin and evolution. Cambridge University Press.

[12] Taylor, G. J. (2013). The bulk composition of Mars. Geochemistry, 73(4), 401-420.

[13] Yoshizaki, T., & McDonough, W. F. (2020). The composition of Mars. Geochimica et Cosmochimica Acta , 273, 137-162.

[14] Cottaar, S., Heister, T., Rose, I., & Unterborn, C. (2014). BurnMan: A lower mantle mineral physics toolkit. Geochemistry, Geophysics, Geosystems , 15(4), 1164-1179.

[15] Stixrude, L., & Lithgow-Bertelloni, C. (2011). Thermodynamics of mantle minerals-II. Phase equilibria. Geophysical Journal International, 184(3), 1180-1213.

[16] Connolly, J. (2009). The geodynamic equation of state: what and how. Geochemistry, Geophysics, Geosystems, 10(10).

[17] Knapmeyer, M. (2004). TTBox: A MatLab toolbox for the computation of 1D teleseismic travel times. Seismological Research Letters, 75(6), 726–733.

[18] Knapmeyer, M. (2005). Numerical accuracy of travel-time software in comparison with analytic results. Seismological Research Letters, 76(1), 74–81.

[19] Bozdag, E., Ruan, Y., Metthez, N., Khan, A., Leng, K., van Driel, M., . . . others (2017). Simulations of seismic wave propagation on Mars. Space Science Reviews, 211(1-4), 571-594.

[20] Bissig, F., Khan, A., Van Driel, M., Stähler, S. C., Giardini, D., Panning, M., . . . others (2018). On the detectability and use of normal modes for determining interior structure of Mars. Space Science Reviews, 214(8), 114.